A Miniaturized Single-Transducer Implantable Pressure Sensor With Time-Multiplexed Ultrasonic Data and Power Links

Marcus J. Weber, *Student Member, IEEE*, Yoshiaki Yoshihara, *Member, IEEE*, Ahmed Sawaby, *Student Member, IEEE*, Jayant Charthad, *Student Member, IEEE*, Ting Chia Chang, *Student Member, IEEE*, and Amin Arbabian, *Senior Member, IEEE*

Abstract—A high-precision implantable pressure sensor with ultrasonic power-up and data uplink is presented. The fully packaged implant measures 1.7 x 2.3 x 7.8 mm^3 and includes a custom IC designed in a 180-nm HV BCD process, a pressure transducer, an energy storage capacitor, and a single piezoelectric transducer (piezo). In order to reduce overall dimensions, unique circuit and system design techniques are presented to enable a single time-multiplexed piezo for both power recovery and data uplink transmission. Implant performance is characterized at significant depths, 12 cm in a tissue phantom, offering a > 13x improvement over state of the art in the depth/volume figure of merit, while demonstrating a robust ultrasonic data uplink with better than 10^{-5} bit error rate. A transient charging analysis is presented to derive the optimal piezo impedance and charging specifications to maximize overall harvesting efficiency. The IC features a front end with a 10-bit SAR ADC achieving a pressure full-scale range of 800 mmHg with a pressure resolution of 0.78 mmHg, exceeding the requirements for a wide range of in vivo pressure sensing applications. The pressure sampling rate is fully externally controlled, up to 1 ksps, in order to significantly decrease implant energy consumption and to allow for adaptable programming for specific applications.

Index Terms—Continuous monitoring, implantable medical devices, implantable sensor, precision health, pressure sensor, ultrasonic communication, ultrasonic power.

I. Introduction

TECHNOLOGY is fundamentally changing how we perform health monitoring, promising to move healthcare from current treatment-based medicine toward more personalized and preventative medicine—a shift that is characterized as a transition from precision medicine to precision health [1], [2]. Today, health monitoring and screening are typically performed during periodic visits to the clinic, providing only brief and infrequent snapshots of a patient's health. In response, there has been increased interest in developing a new technologies to allow for continuous *in vivo* monitoring outside of the clinic with the goals of better understanding disease dynamics as well as to enable early detection. Ultimately, this will allow for more preventative and targeted treatments with more favorable outcomes and lower healthcare costs [1], [2].

Among the many physiological parameters of interest, pressure is an important metric for determining the health of various organs and biological systems throughout the body [3]–[8]. For example, pulmonary artery pressure is used for diagnosing cardiovascular issues [6], bladder pressure is measured for treatment of incontinence [7], and intraocular pressure is monitored for diagnosing and managing glaucoma [8]. Pressure measurements are commonly used for clinical diagnosis and monitoring, but the limited data gathered from sparse clinical screenings often does not characterize minimum and maximum pressure variations or information in how pressure changes over time. Currently, catheterization is used clinically for long term and localized pressure sensing, but this restricts the patient to a bed and requires piercing the skin, which can lead to infection [3]–[5]. Techniques for measuring pressure noninvasively have also been investigated, but they do not provide adequate precision or localized pressure [3], [7]. Therefore, there is a need for development of minimally invasive, fully wireless pressure sensors for continuous monitoring of many different pressures throughout the body, including blood, bladder, intra-abdominal, intracranial, and intraocular pressure [3]–[5].

Collectively, the major *in vivo* pressures span a range of roughly −10 to 200 mmHg, referenced to atmospheric pressure with a target pressure resolution of ±1 mmHg [3], [4], resulting in a requirement of 8-bit precision or higher when considering atmospheric changes, noise, and other nonidealities and variations. There is also a large range in the required signal bandwidth for different pressures. For example, some blood pressure sensing applications can require up to 100s of hertz, while other applications require hertz or even sub-hertz bandwidth [3]. On top of these sensing requirements, scaling down implant size to millimeter dimensions is

M. J. Weber, A. Sawaby, J. Charthad, T. C. Chang, and A. Arbabian are with the Electrical Engineering Department, Stanford University, Stanford, CA 94305 USA (e-mail: mjweber3@stanford.edu; asawaby@stanford.edu; jayantc@stanford.edu; tcchang3@stanford.edu; arbabian@stanford.edu).

Y. Yoshihara was with Stanford University, Stanford, CA 94305 USA. He is now with Toshiba Memory Corporation, Kawasaki 212-8520, Japan (e-mail: yoshiaki.yoshihara@toshiba.co.jp).

of critical importance to reduce the invasiveness of surgery and to improve overall long-term biocompatibility. Many applications like bladder, blood, and intra-abdominal sensing also necessitate great implantation depths (>10 cm), while requiring energy efficient wireless powering and reliable data links. These specifications present the significant challenge of designing a high-precision implantable sensor with millimeter-form factor, capable of operating wirelessly at >10 cm in tissue.

In recent years, there has been significant research progress into the development of wireless implantable sensors for many applications, such as neural recording [9]–[12], glucose monitoring [13], temperature sensing [14], pH sensing [14], [15], and pressure sensing [6], [8], [14], [16]–[26]. The vast majority of these sensors utilize inductive or RF links for power and data delivery. As an alternative approach, we utilize ultrasonic links for both power delivery and data transmission, due to a few important advantages. Ultrasound (US) has smaller wavelengths in tissue (e.g., $\sim$1.5 mm at 1 MHz) allowing for: 1) highly directive focusing down to millimeter spots at great depths (>10 cm) [27]–[29] and 2) high acoustic-electrical efficiency with millimeter-sized receivers [30]–[32]. In addition, US signals experience lower tissue attenuation ($\sim$0.5–1 dB/cm·MHz) [33]. These advantages are key to scaling down implant size while also enabling for high efficiency power transfer and data links for great tissue depths.

A few US-powered implants have already been shown in the literature for electrical stimulation [34], [35], optical stimulation [32], neural recording using a US backscatter [36], oxygen generation [37], and data transmission [31], [38]; however, a fully ultrasonic high-precision sensor has yet to be demonstrated. Toward this goal, we present a miniaturized, high-precision implantable pressure sensor with US power and data links. This paper builds on work described in [39], but proposes an entirely new implementation using a single piezoelectric transducer (piezo) for both power recovery and data transmission, to further shrink form factor. Circuit and system design techniques are presented for solving the unique challenges posed due to operation with a single piezo. We also expand on the material in [39] with new measurements, analysis, and circuit descriptions. The implant is wirelessly tested at 12 cm of depth in a tissue phantom and demonstrates a robust 30 dB SNR uplink. The pressure sampling rate (f_s) is controlled externally, reducing energy consumption by eliminating continuously running support circuitry. The fully packaged implant measures just $1.7 \times 2.3 \times 7.8$ mm^3 and achieves a $> 13\times$ improvement over state of the art in the depth/volume figure of merit (FoM).

This paper is organized as follows. In Section II, we discuss the system-level blocks, external sampling control, and a time multiplexing (TM) scheme used for power, sensing, and data uplink. The power management (PM) and a US power detector block are described in Section III. In addition, we present an analysis used for optimizing the impedance match efficiency during the transient power-up phase. In Section IV, we present the data transmitter design including unique circuit techniques we used to enable the single piezo implementation. The co-design of the piezo and matching network are shown
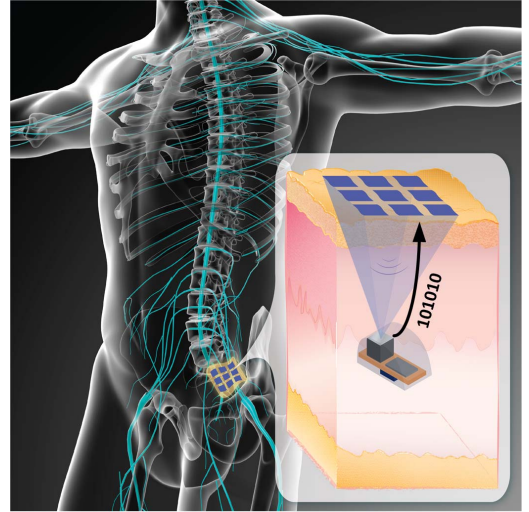

Fig. 1.   Conceptual image of fully ultrasonic implantable pressure sensor system.
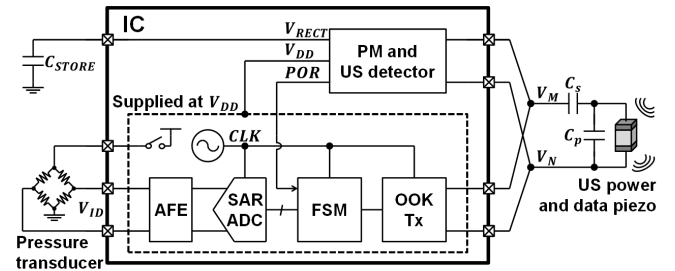

Fig. 2.   Block diagram of the implantable pressure sensor.

in Section V. In Section VI, we discuss design of the analog-to-digital signal path. Finally, the implant performance is then characterized using a modular fully wireless setup (Section VII) and in fully packaged form (Section VIII).

II. System Level Description

A conceptual diagram of the proposed system is shown in Fig. 1, consisting of the implantable sensor and an external transceiver. The external transceiver beams US power to the implant, and the implant samples pressure and returns the measurement in digital format via the US data uplink. In this paper, we focus on design of the implantable sensor and use commercial US transducers for the external transceiver. Fig. 2 shows the block diagram of the implantable pressure sensor, which is comprised of four main components: 1) the piezo with L-match capacitors; 2) a resistive bridge pressure transducer (PT); 3) a storage capacitor (C_{STORE}); and 4) the IC. The IC consists of several circuit blocks, including: PM and US power detection circuits, an analog front-end (AFE), a 10-bit SAR ADC, a finite-state machine (FSM), a relaxation oscillator, and an on-off keying (OOK) data transmitter (Tx).

The piezo and matching network are co-designed to both recover US power and transmit US uplink data, and thus, are directly connected to both the PM and the OOK Tx blocks. To enable single piezo functionality, a TM scheme
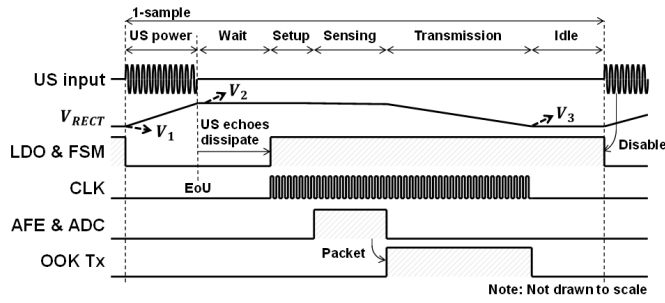
Fig. 3. Implant TM scheme for US power, sampling, and data transmission.

between US power and data uplink is utilized to mitigate interference. In addition, in the preliminary characterization of the PT, we found that US can couple to the PT output signal and corrupt the sample, especially with the large required dynamic range in this application. This issue is unique to US power systems. Therefore, we extended the TM approach to sequentially schedule: 1) US power-up; 2) pressure sensing; and 3) US data uplink.

The TM timing diagram is shown in Fig. 3. Operation begins when the implant receives a US power burst from the external source; the incoming US energy is harvested and stored on C_{STORE} as V_{RECT} – charging from V_1 to V_2 (annotated in Fig. 3). The onset of the US burst is also detected by a US power detector circuit, which disables the low-dropout regulator (LDO) to lower energy consumption. After the end of the ultrasound burst (EoU), the US power detector senses the falling edge of the envelope, triggering the beginning of the implant operation. This process begins by sending the implant into a sufficiently long waiting period ($\sim$200 μs) to allow for the US power echoes to dissipate, in order to avoid US coupling to the PT during sampling. Next, the LDO is enabled and the FSM is reset via a power on reset signal once the LDO has stabilized. The oscillator is started and after a short initialization period, the pressure sensing phase begins. The AFE samples the pressure readout from the PT, and then the sample is digitized through the 10-bit SAR ADC. Finally, the sample is serialized and transmitted through the piezo (US uplink data) using an OOK modulation, concluding implant operation. At this point, V_{RECT} will be depleted down to V_3; therefore, the energy storage must be great enough to prevent V_3 from falling below the LDO compliance voltage ($V_{RECT,min}$) to prevent the LDO from going into dropout during implant operation. The implant then returns to an idle state where it waits indefinitely for the next US power burst. In the idle state, all blocks sourced by the LDO are shut down and only the LDO quiescent current and a few current biases are left on. A low carrier frequency (790 kHz) is used for both the power and data uplink to minimize the link loss ($\sim$0.5–1 dB/cm $\cdot$ MHz) [33], allowing for efficient operation at great depths ($>$10 cm).

As shown in the Fig. 3, the implant returns a single pressure sample per incoming US power burst; therefore, f_s is controlled exclusively by the external transceiver through modulation of the US burst repetition rate. For example, an US burst repetition rate of 1 kHz will result in 1-ksps pressure sampling. Thus, the US power burst serves two functions:

1) the burst must provide enough harvested energy for the implant to sample and return the pressure data and 2) the falling edge of the burst initializes the sampling process, acting as the downlink f_s control. The total implant operation time, from US power to data transmission, is limited to $<$1 ms to enable up to a 1-ksps f_s. While we designed the implantable sensor to operate up to 1 ksps, many pressure sensing applications require only 1 to tens of sps [3]. These low f_s are many orders of magnitude below mixed-signal IC capabilities. In response, designers typically duty-cycle the power-intensive blocks to reduce energy consumption [16], [18], [20]. However, even low-power oscillators and supporting circuits, used for implant power, timing, and logic, can dissipate significant amounts of energy over long millisecond to second time scales. By pushing the sampling rate logic and control onto the external transceiver, we avoid the need for these continuously running circuits, on the implant, while in the idle state. This significantly reduces implant energy consumption, especially at low f_s (as shown in Section VII), and allows the implant to remain in the idle state indefinitely, without need for an energy source. Instead, all of the energy needed to sample and return the single pressure sample is supplied by the single US burst. The transceiver can more efficiently control the sampling logic, and allows for the possibility of running dynamic and adaptive tuning algorithms of the sampling rate, based on the real-time data and trade-off with system energy consumption. In addition, the external transceiver is time synchronized to the implant since a sample is returned after each US burst; therefore, the external receive path can be duty-cycled to reduce energy overhead on the transceiver.

III. POWER MANAGEMENT AND US POWER DETECTOR

A. PM Architecture

A diagram of the PM block and US power detector is shown in Fig. 4(a). The piezo was designed with sufficiently high impedance to achieve large harvested voltages [30], [32], much greater than diode thresholds ($V_{DIODE} \cong$ 300–350 mV), allowing for the use of a Schottky full-wave bridge-rectifier for voltage rectification. AC clamps at the input of the rectifier and dc clamps on V_{RECT} are used to limit the rectifier input (V_{MN}) and V_{RECT} ($<\sim$4 V) to prevent breakdown of the devices. The BJT-based bandgap reference (BGR) is used to create a reference voltage (V_{REF}) and current for various blocks on the IC. The BGR consumes 800 nA of current. The LDO supplies all circuits outside of the PM at $V_{DD} \cong$ 1.9 V, including the oscillator, FSM, AFE, SAR ADC, and OOK transmitter. A PMOS pass transistor was used for LDO, allowing for a $V_{RECT,min}$ of $\sim$2 V. The LDO draws 6 μA of quiescent current.

B. US Power Detector Design

A parallel US power detector path is used to implement the $\sim$200-μs US echo wait time after the EoU, and to disable the LDO during the US power and wait time phases to conserve energy. The US detector consists of a current mirror comparator with rail to rail output swing and a charge integration-based
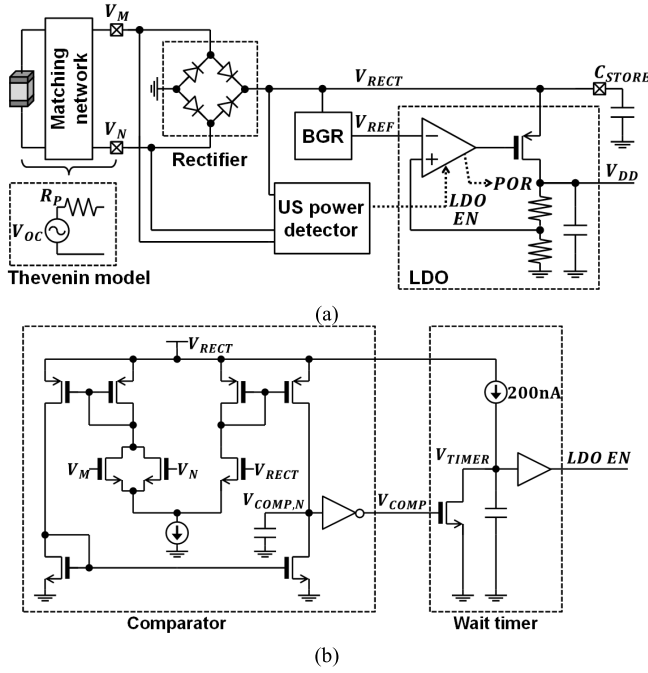
Fig. 4. (a) Diagram of the PM unit and US power detector. (b) Schematic of the US power detector consisting of an analog comparator and charge integration wait timer.

wait timer, as shown in Fig. 4(b). A charge integrator wait timer is used, as opposed to an oscillator, since a precise wait time is not required, and it consumes only 200 nA. The analog comparator monitors the input of the rectifier and compares with V_{RECT} to sense the US power burst. At the start of the US power burst, the comparator output (V_{COMP}) swings high, discharging the wait timer capacitor node (V_{TIMER}), and disables the LDO (i.e., LDO EN goes low). Extra capacitance is added at $V_{COMP,N}$ to filter high-frequency transitions, requiring a few cycles to charge and discharge $V_{COMP,N}$, in order to prevent $V_{COMP,N}$ from swinging high during the brief times when V_M, V_N < V_{RECT} during power-up. At the EoU, V_{COMP} swings low, starting the charge integration timer, and when V_{TIMER} exceeds the output buffer threshold, the LDO EN signal is pulled high, starting the LDO. Since the input of the rectifier is directly connected to the OOK Tx, V_{RECT} is used for comparison with V_M and V_N in order to differentiate between the US power burst and the uplink data transmission, which has peak amplitude of V_{DD} < V_{RECT}. This is necessary to avoid an erroneous restart of the LDO during data transmission.

C. Charging Efficiency Analysis

In order to maximize harvesting efficiency, the harvester impedance needs to be tuned to achieve an efficient effective impedance match with the non-linear and time-dependent power electronics [30], [31], [40], [41]. To implement the TM scheme, we utilize a transient charge-and-store approach, as opposed to the more common case of directly powering the implant during operation [19], [20], [31], [32]. For direct powering, the transient phase is typically ignored and the

impedance match is optimized for the steady-state operation by using an effective time averaged or constant load assumption. However, this technique is not directly applicable with the transient charge approach since the piezo provides energy to a time-varying load with no periodic average effective impedance, as V_{RECT} charges from V_1 to V_2 shown in Fig. 3. Consequently, we present a numerically solved transient charging analysis to investigate the optimal harvester impedance.

During periodic sampling, the total implant energy dissipated per pressure sample (E_{SAMP}) must be replenished during the subsequent US power-up phase in order to allow the implant to continuously function. The total energy dissipated per pressure sample is $E_{SAMP} = E_{OPER} + E_{IDLE} = 1/2 C_{STORE} (V_2^2 - V_1^2)$. E_{OPER} is the energy dissipated during chip operation. E_{IDLE} is the idle phase energy dissipation, which is composed mostly of the bias current sources and the LDO quiescent current. E_{IDLE} varies drastically with f_s (i.e., time spent in idle state)—small for high f_s, but becomes significant for low f_s. For very low f_s, E_{IDLE} can completely deplete C_{STORE} ($V_1 = 0$); therefore, C_{STORE} limits the maximum energy to $E_{SAMP,max} = 1/2 C_{STORE} V_2^2$. C_{STORE} must be sized large enough to maintain V_{RECT} above the LDO compliance voltage ($V_{RECT,min}$), and sufficiently below the V_{RECT} clamping voltage ($\sim$4 V), while dissipating E_{OPER} during operation (i.e., $V_{RECT,min}$ < V_2, V_3 < 4 V). However, C_{STORE} should be limited in size to reduce $E_{SAMP,max}$ for lower f_s. Therefore, we chose $C_{STORE} = 80$ nF in order to supply $E_{OPER} \cong 100$ nJ while limiting the E_{SAMP} for low f_s, as will be shown in Section VII.

The Thevenin equivalent model for the combined piezo and matching network, operating at resonance, is shown in Fig. 4(a), consisting of an open-circuit voltage ($V_{OC} = (8 \times R_P \times P_{AV})^{1/2}$) and source resistance (R_P)—where P_{AV} is the electrical available power [30]. We can model the PM block as a rectifier with a capacitive load since the IC load is negligible during charging. Using these models, along with a constant diode drop assumption ($\sim$350 mV) for the bridge-rectifier, we can compute the harvested charge per cycle, as a function of P_{AV}, R_P, and V_{RECT}. Recursively solving over many cycles, the required charging time (T_{CHARGE}) for charging C_{STORE} over an arbitrary range of V_1 to V_2 can be found for given P_{AV} and R_P. The charging efficiency (η_{CHARGE}) is defined as the ratio of E_{SAMP} to the product of P_{AV} and T_{CHARGE}, or mathematically as

$$\eta_{CHARGE} = \frac{E_{SAMP}}{P_{av} \times T_{CHARGE}}. \qquad (1)$$

The computed T_{CHARGE} and corresponding η_{CHARGE} for $R_P = 3$, 10, and 30 kΩ swept over P_{AV} are shown in Fig. 5. These results were plotted with example values $V_1 = 2.1$ V and $V_2 = 2.65$ V, to be compared with the measurement results in Section VII, though any V_1 and V_2 can be used in our analysis framework. Based on these results, for each R_P, there exists an optimal charging P_{av} and T_{CHARGE} for achieving maximum η_{CHARGE}. As can be seen, the maximum $\eta_{CHARGE} = 70\%$ is roughly constant over a wide range of R_P, at least from 3 to 30 kΩ, demonstrating that there is no single R_P for maximizing the effective impedance match. In this case, T_{CHARGE}
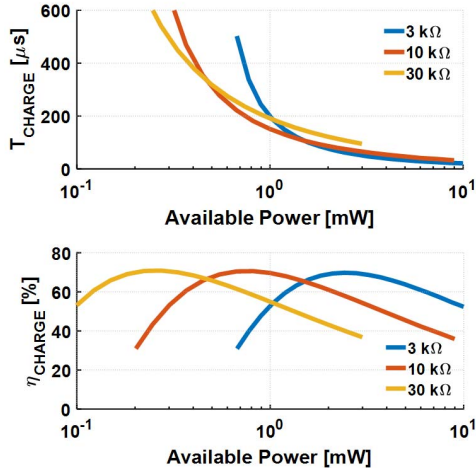
Fig. 5. Computed charging time and efficiency as a function of available power for a given effective source resistance.

offers another variable, which can be tuned to optimize the effective impedance match. This result illustrates a stark difference between transient charging versus direct, steady-state powering where there typically exists a narrow range of optimal R_P and P_{AV} to maximize the effective impedance match. The optimal T_{CHARGE} increases roughly linearly with R_P since the optimal P_{av} decreases; therefore, T_{CHARGE} must also be considered when selecting R_P.

In summary, the results shown in Fig. 5 can be used for deriving the design specification for the piezo impedance and optimal P_{AV} based on requirements for η_{CHARGE} and T_{CHARGE}. It is important to note that this analysis is applicable to any harvesting transducer, which has a similar linear Thevenin model including antennas and inductive coils. In this design, the single piezo functions as both the power harvester and the data uplink transmitter; consequently, additional data uplink design specifications are imposed on the piezo, as described in the following sections.

IV. DATA TRANSMITTER DESIGN FOR SINGLE PIEZO

In [38], we utilized a frequency duplex scheme for US power and data along with a 2.45-MHz carrier frequency in order to demonstrate a higher data rate (95 kb/s) uplink at 8.5-cm depth. While higher carrier frequencies can offer greater bandwidth, and thus data rate, US tissue attenuation scales with frequency (∼0.5–1 dB/cm·MHz) [33], giving a trade-off between data rate and link efficiency. Based on the pressure sampling rate (up to 1 ksps) and the desired sensing resolution (10 bit), the pressure sensing application requires a maximum of ∼10 kb/s, which is well below the bit rates shown in [38]. Therefore, we utilize a lower carrier frequency (790 kHz), along with the TM scheme for power and data uplink, to meet the required data rate, while allowing for extension of the operational depth to greater than 12 cm.

A relaxation oscillator is designed to generate the 790-kHz carrier frequency for uplink data. To reduce the process and supply dependent variation of the 790-kHz frequency, an all NMOS current generator, along with all NMOS relaxation threshold detection, were used. The transmitter utilizes a
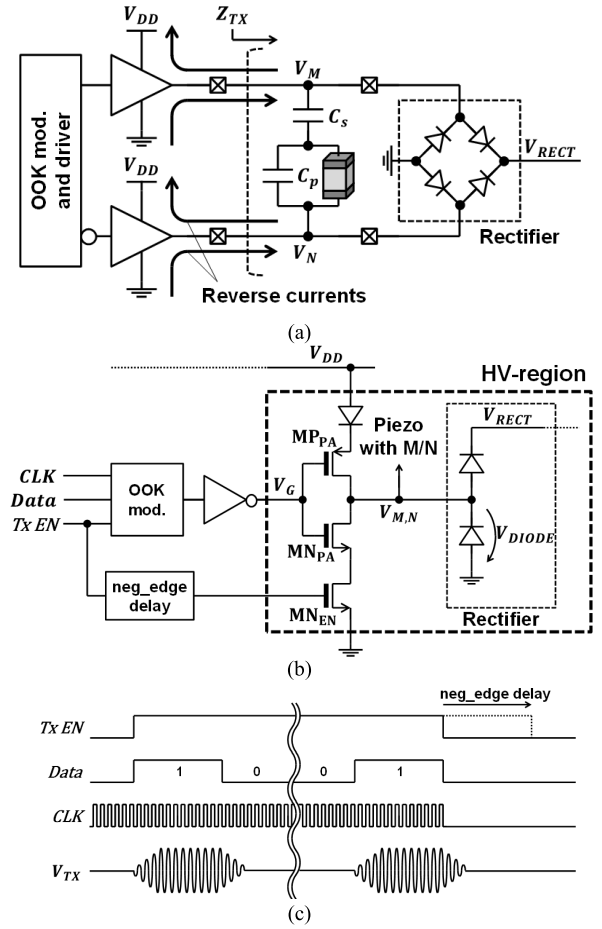

Fig. 6. (a) Diagram showing piezo connections to the PA and rectifier (expanded from Fig. 2) with undesirable reverse currents annotated. (b) Single-ended schematic of modified class-D PA. (c) Data Tx timing diagram.

modified differential class-D power amplifier (PA) with OOK modulation. The PA is voltage limited and allows for trading off the radiated uplink power and implant energy dissipation by changing the impedance of the effective piezo load. For instance, we can increase radiated power for operation at great depths (>10 cm) or decrease power for shallow depths. In preliminary measurements of the US data link, using various piezo designs for transmit and a commercial US transducer for receive, we found that ∼100 μW of radiated power was required to achieve a high SNR (∼30 dB) at >10 cm in tissue phantom. Therefore, we targeted 100 μW in order to demonstrate a robust US data uplink, at great depth, with significant SNR margins in this proof-of-concept system.

Since we are utilizing a single piezo for both power and data, the output of the PA, the input of the rectifier, and the matching network with the piezo are connected in parallel, as shown in Fig. 6(a). As such, the PA must be specially designed to block any reverse current paths flowing through the output PA to V_{DD} or GND during US power-up. For instance, currents flowing through the PA to V_{DD} would result in undesired charging of the LDO capacitor by the piezo, beyond V_{DD}, leading to breakdown of the low-voltage devices connected to the LDO. Current paths to GND must also be

blocked to prevent shorting of the piezo during US power-up. These challenges are further complicated since they must be averted without the use of a proper and robust V_{DD} or logic because the implant must be able to startup without any stored energy. In addition, in the case that the implant still has stored energy and a stable V_{DD}, the LDO will be disabled upon receiving the next US power burst; therefore, the V_{DD} will decrease below the nominal regulated value during charging (see Fig. 12). To illustrate the techniques used to block these current paths, a simplified, single-ended version of this circuit is shown in Fig. 6(b).

During the charging phase, $V_{M,N}$ is clamped by the Schottky rectifier, swinging between $V_{RECT} + V_{DIODE}$ and $-V_{DIODE}$. We used 5-V HV-devices for the output stage of the PA in conjunction with ac clamps to limit $V_{M,N}$ below 5 V to prevent breakdown. To block any currents to or from the piezo during power-up, we modified the conventional class-D PA by adding a Schottky diode between V_{DD} and MP_{PA} and an enable NMOS switch (MN_{EN}), which is switched off when not transmitting data. In addition, the gate voltage (V_G) to the output inverter is pulled up to V_{DD} during US power-up, and will track V_{DD} as it decreases during charging. To demonstrate the power-up current blocking function of the modified class-D amplifier, it is convenient to consider three different ranges for $V_{M,N}$: 1) $-V_{DIODE} < V_{M,N} < 0$; 2) $0 < V_{M,N} < V_{DD}$; 3) and $V_{M,N} > V_{DD}$. Using these different Cases 1)–3), we can evaluate the bias of the top PMOS path and the bottom NMOS path to ensure they are appropriately open circuited.

Case 1: When $-V_{DIODE} < V_{M,N} < 0$, the top path is off since MP_{PA} is in cutoff. In the bottom path, MN_{PA} is on, but MN_{EN} is sufficiently in cutoff since the V_{GS}, $V_{GD} \leq V_{DIODE}$, which is much less than an NMOS threshold voltage (V_{TN}).

Case 2: When $0 < V_{M,N} < V_{DD}$, the top path is off since MP_{PA} is in cutoff. In the bottom path, MN_{PA} will turn on for $V_G - V_{M,N} > V_{TN}$, but MN_{EN} operates in cutoff.

Case 3: When $V_{M,N} > V_{DD}$, MP_{PA} will turn on for $V_{M,N} - V_G > |V_{TP}|$, but the Schottky diode is reverse biased, open circuiting the top path. Both MN_{PA} and MN_{EN} are in cutoff in the bottom path.

Therefore, in all operating conditions, the PA will block any currents from the piezo during the charging phase.

The timing diagram for data transmission is shown in Fig. 6(c). During the data transmission phase, the Tx EN goes high, enabling the bottom NMOS in the PA. The reverse current protection Schottky diode comes at the cost of slightly decreased PA efficiency due to the diode drop. An added advantage of using the passive Schottky rectifier is that the diodes in the rectifier block any $V_{M,N} < V_{RECT} + V_{DIODE}$; therefore, it does not electrically load the PA during transmission. The final modification consists of the negative edge (neg_edge) delay block. This block is used to temporarily short both terminals of the piezo to GND after the data transmission has ended (Tx EN goes low) to dissipate residual energy stored in the piezo after data transmission.

V. PIEZO DESIGN

The ultrasonic and electrical characteristics of a piezo, such as the frequency, impedance, and effective aperture, are
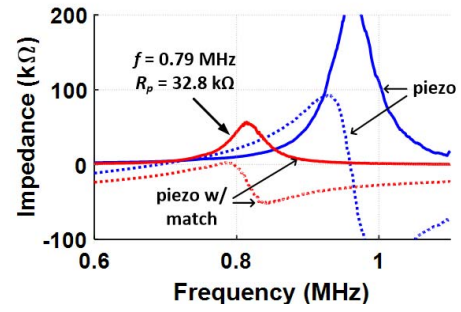

Fig. 7.   Measured impedance profile of the piezo with and without the matching network. Note that the solid and dotted lines represent the real and imaginary components, respectively.

primarily determined by the piezoelectric material, thickness, and cross-sectional area. For piezo fabrication, we utilize commercially available piezoelectric plates of a chosen thickness and dice out the desired piezo area according to the specifications. We have presented detailed piezo design techniques and methods in [30] and [42]. In this application, we design the piezo such that it operates in the inductive impedance band [30], between the short-circuit (f_{sc}) and open-circuit (f_{oc}) resonance frequencies. This technique allows us to use the inherent inductance of the piezo, along with small capacitors for matching, to fine tune the impedance and resonance frequency. PZT-5A material is chosen because it has a relatively low sound velocity [43], yielding lower resonance frequencies for a given thickness. A thickness of 1.8 mm is used to position the 790-kHz carrier frequency within the inductive band. A cross section of 1.1 mm × 1.1 mm was chosen for small area (i.e., smaller than IC) while still providing significant US aperture area. Given a targeted radiated power of ~100 μW, we can compute the specification for impedance seen by the PA (Z_{TX}) to be ~30 kΩ—assuming narrowband operation. A capacitive L-match network ($C_S = 15.2$ pF and $C_P = 5.6$ pF) is used to increase the effective resistance and the shift resonance frequency to 790 kHz—meeting the specification. The measured impedance profiles of the piezo with and without the matching network are shown in Fig. 7. An air-backed package, similar to what is described in [38], was used for increased US-to-electrical aperture efficiency. The US-to-electrical aperture efficiency was measured to be 40%.

VI. PRESSURE SIGNAL PATH

Our goal was to build a general purpose pressure sensor suitable for most major *in vivo* pressure monitoring applications, including intraocular, intracranial, blood, bladder, and intra-abdominal pressures [3], [4]. Typical reported values for the maximum pressure full scale (P_{FS}) and resolution for these various applications are 200 and ±1 mmHg, respectively [3], [4]. We designed to exceed these metrics while also accounting for atmospheric pressure changes due to elevation; therefore, we targeted a $P_{LSB} < 1$ mmHg, for noise margin, and an absolute pressure range beyond 560–1000 mmHg, giving a $P_{FS} > 440$ mmHg. We chose the SM5108C piezoresistive PT due to its extremely small form factor (650 μm × 650 μm × 650 μm). Several of the SM5108C PT were
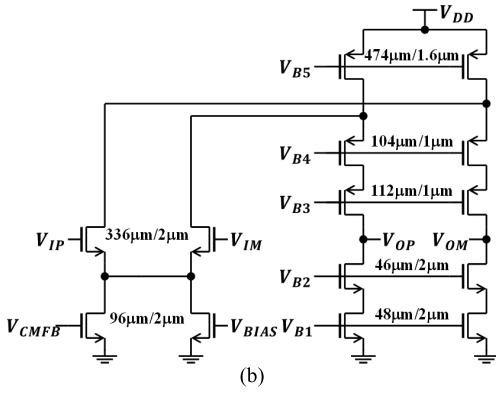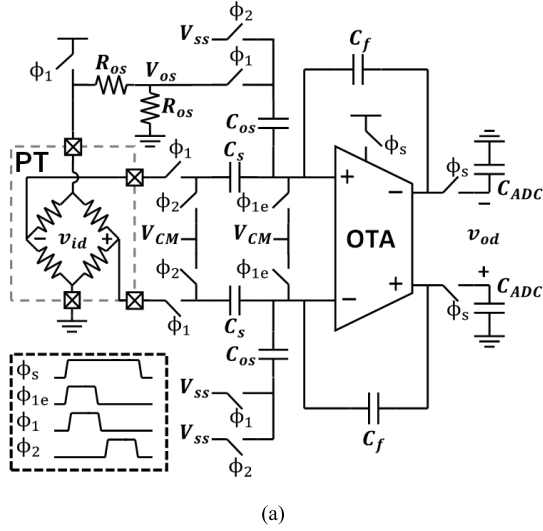
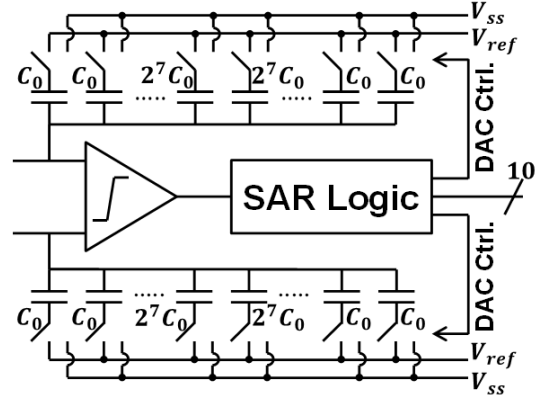Fig. 8. (a) Schematic of the AFE and the (b) modified folded-cascode OTA.

Fig. 9. Schematic of 10-bit SAR ADC with constant-common mode switching scheme.

following AFE transfer function:

$$v_{\text{od}} = \frac{C_s}{C_f} v_{\text{id}} - \frac{C_{\text{os}}}{C_f} V_{\text{os}}. \tag{2}$$

The OTA was implemented using a folded-cascode topology with an additional PMOS cascode stage, as shown in Fig. 8(b). The extra PMOS stage increases the G_m/I efficiency of the OTA by dropping the impedance seen looking into the cascode PMOS, forcing the signal current to the output. Current in the second branch can then be further reduced without losing significant G_m. The input pair was sized to 336 μm/2 μm for large g_m/I_d and to reduce offset. To allow for fast front-end settling time, a slew-rate enhancement common-mode buffer is used to generate V_{CM}. This helps in charging the large front-end/sensor caps ($C_s = 49.5$ pF and $C_f = 2.2$ pF) in a fast and energy efficient manner.

B. SAR ADC Design

The 10-bit SAR ADC, shown in Fig. 9, was implemented with a top-plate sampled, constant common-mode capacitive DAC [45]. To ensure high ADC linearity and mitigate parasitic capacitance (i.e., gain loss), the capacitor DAC is built using custom-made metal-oxide-metal (MOM) capacitors on the top most thin-metal layer [46]. Since the capacitor DAC area is relatively large, dummy MOM capacitors were used to avoid the rise of second order effects such as metal dishing. The comparator was implemented using the StrongARM latch topology. A 500-mV SAR ADC reference was generated using a dedicated sub-BGR generator, giving an LSB of ~1 mV. As opposed to the PM BGR, which was optimized for energy, the SAR reference was optimized for accuracy, and is disabled when the SAR is not operating to conserve energy.

VII. IMPLANTABLE SENSOR CHARACTERIZATION

We fabricated the IC using the Taiwan Semiconductor Manufacturing Company 180-nm HV BCD process for circuit compatibility with high-voltage implantable applications such as electrical stimulation. The chip measures 1.86 mm × 0.95 mm and the die photograph is shown in Fig. 10. The LDO capacitor, consisting of both MIM and MOS capacitors, is large (1.3 nF), so it was tiled around the other circuit blocks to provide localized decoupling capacitance for each block.

measured in order to characterize variations in sensitivity and offset between samples. We measured sensitivities between ~26–30 μV/(V·mmHg) and found up to a few mV offset between samples. Ultimately, we decided on a conservative 10-bit design, allowing for significant full-scale margin to account for PT variations while also meeting the P_{LSB} spec.

A. Analog Front-End Design

A 27-dB gain switched-capacitor AFE was used to sample and amplify the pressure signal from the PT, as shown in Fig. 8(a). The PT and OTA bias are duty-cycled on only during sampling in order to conserve energy. Both the PT and OTA are started during ϕ_1, allowing for the PT signal to settle on C_s and for the OTA to establish bias. During ϕ_2, the PT is shut off to conserve energy and the signal is amplified and stored on the SAR DAC (C_{DAC}). Both phases last for two clock cycles. In addition, duty-cycling of the OTA bias is also used to mitigate flicker noise, as described in [44]. Low-frequency front ends typically use chopping or auto-zeroing; however, this method of flicker noise reduction is sufficient in this design since we only sample a single time (i.e., short OTA bias time). Since the pressure sensor is referenced to vacuum, we added an offset path (V_{os}) and size C_{os} to center the input V_{FS} range near the ADC center word, giving the
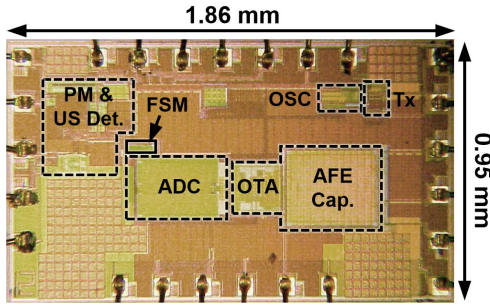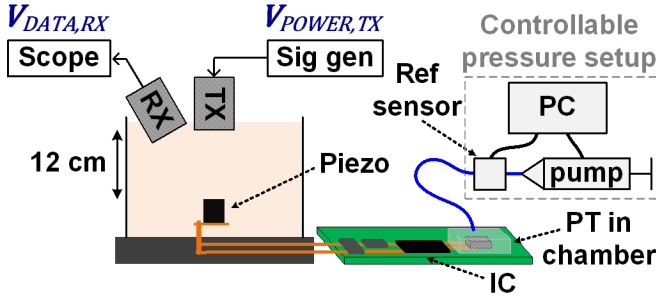
Fig. 10. Die photograph of the IC.

Fig. 11. Characterization setup used for detailed probing of the implantable sensor internal nodes. US power and data are transmitted through 12 cm of tissue phantom, and a controllable pressure setup is used to vary pressure.

To fully characterize the system, as a first step, we utilize the modular setup shown in Fig. 11, which allows us to perform wireless ultrasonic measurements while giving access to internal nodes of the implantable sensor. This setup also enables us to isolate the PT so that we can precisely control the pressure level. We will describe testing with the fully packaged implant in the following section. For the ultrasonic power and data links, the piezo is bonded onto a small PCB and placed in a tank filled with castor oil, which acts as a tissue phantom ($\sim$0.6 dB/cm·MHz). Commercial transducers are placed at the top of the tank for US power transmission ($V_{\text{POWER,TX}}$) and receiving of the uplink data ($V_{\text{DATA,RX}}$)—the RX is placed at a $\sim$20° angle. All wireless measurements were conducted through 12 cm of castor oil. Traces are routed outside of the tank connecting the piezo to an external PCB, which includes the matching capacitors, IC, and the PT. The PT is placed in a 3-D printed chamber and connected to a custom built, air-tight controllable pressure setup built from microfluidic components. The pressure setup includes a PC-interfaced syringe pump for accurate control of the pressure levels. We also included a high-precision reference sensor with better than 0.01-mmHg resolution for benchmarking the implantable pressure sensor measurements.

A. Fully Wireless Characterization

Fig. 12 shows the fully wireless end-to-end measurement of the implantable system for two samples at 1 ksps. The magnitude of the voltage ($|V_{\text{MN}}|$) across the single piezo and matching network shows the incoming US power burst, and later on during operation, the US data uplink. The US power burst was 150 cycles at 790 kHz, giving a T_{CHARGE} of 190 μs,

and provided an electrical available power of 990 μW. The time averaged US intensity required for implant operation was 400 μW/mm^2, which is just 5.5% of the FDA diagnostic limit of 7.2 mW/mm^2 [47]. The total energy per sample is $E_{\text{SAMP}} = 104.5$ nJ, composed of an $E_{\text{OPER}} = 101.1$ nJ and $E_{\text{IDLE}} = 3.4$ nJ ($E_{\text{OPER}} \gg E_{\text{IDLE}}$ since we are using high f_s). Based on the analysis shown in Fig. 5, the maximum η_{CHARGE} for an $R_P \cong 30$ kΩ is achieved with an optimal $P_{\text{AV}} \cong 300$ μW and $T_{\text{CHARGE}} \cong 500$ μs. Here we charged at a higher P_{AV} to get a shorter T_{CHARGE} for demonstrating 1 ksps. While operating slightly off the optimal charging point, we were still able to achieve a η_{CHARGE} of 55%, in agreement with Fig. 5, which is $\sim$15% lower than optimal. The US echo wait time was measured to be 210 μ s, after which the LDO started and settled to a value of 1.94 V. The sensor ($V_{\text{DD,SEN}}$) is activated for 2.5 μs during ϕ_1, shortly after the LDO starts.

The bottom graph in Fig. 12 shows the measured $V_{\text{DATA,RX}}$ at the external RX, achieving a 30-dB SNR data uplink. There is a $\sim$82-μs delay between the data transmission and received data, which corresponds to a 12-cm depth. Each transmitted data packet consists of a "10" preamble followed by the 10-bit code—the code is 478 for these two samples. Note that $V_{\text{DATA,RX}}$ also shows a received signal from US backscattered off of the implant during power-up, but this is spaced far from the uplink data signal using the TM scheme. To further characterize the data uplink, we performed bit error rate (BER) measurements using the setup shown in Fig. 11. Bit-errors were assessed by monitoring the SAR ADC output code and comparing with the received $V_{\text{DATA,RX}}$ waveform. The measurement was error free over all 10^4 samples (120 kb), yielding a BER less than 10^{-5}, and demonstrating a reliable communication link up to 12-cm depth in tissue phantom.

We also performed implant characterization at lower f_s to illustrate the low-energy operation obtained using the externally controlled sampling scheme. Fig. 13 shows the measured E_{SAMP} and E_{IDLE} as a function of f_s. For each measurement, we charged V_{RECT} to the same $V_2 = 2.65$ V and held the output code fixed to ensure E_{OPER} was constant for each f_s; hence, the increase in E_{SAMP} with decreasing f_s is entirely due to increased E_{IDLE}. As discussed in Section III-C, $C_{\text{STORE}} = 80$ nF was chosen as a trade-off between energy storage capacity for E_{OPER} and for limiting the maximum E_{IDLE} in the idle state; therefore, we only see a modest increase in E_{SAMP} as a function of decreasing f_s. For $f_s = 1$ sps, C_{STORE} was fully depleted ($V_1 = 0$ V) at the beginning of every charging cycle, requiring $E_{\text{SAMP}} = 280$ nJ and limiting the maximum E_{IDLE} to just $\sim$180 nJ. Therefore, we see only a $\times$50 increase in E_{IDLE} over a three-decade span of f_s while we would expect a near linear relationship (i.e., 1000$\times$ increase) if continuously running logic, timing, or support circuits were required during the idle phase. For even lower sampling rates, the E_{SAMP} remains fixed at 280 nJ as indicated by the dashed line. These results illustrate a significant energy advantage of fully pushing control of the sampling rate and logic to the external transceiver, as shown in Table I.

The average power consumption for the external source was measured to be 800 mW for 1 ksps and decreased to just 2.2 mW for 1 sps. It is important to note that we did
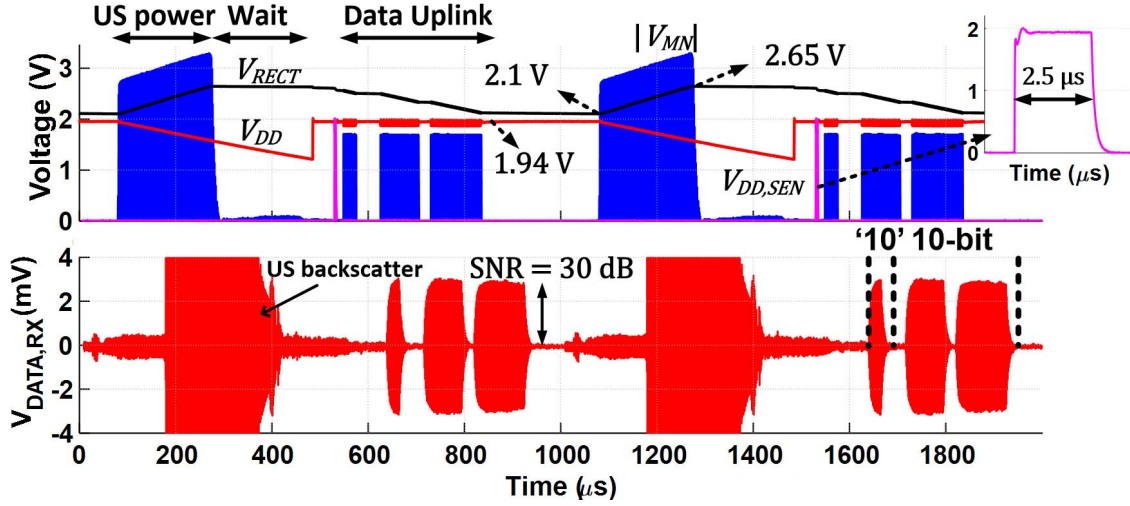
Fig. 12. Wireless measurement showing the full end-to-end operation of the implantable pressure sensor over two consecutive samples ($f_s = 1$ ksps). The total energy per sample is 104.5 nJ and a 30-dB SNR data uplink is shown for robust communication.
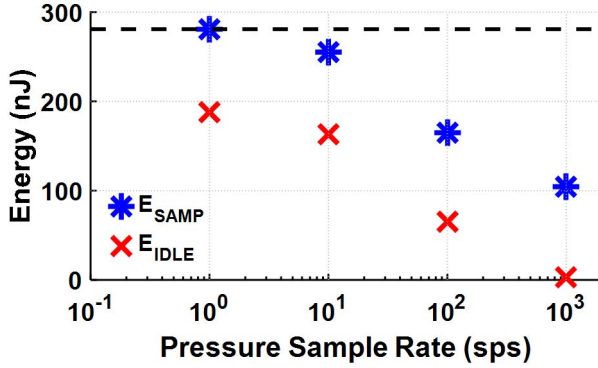

Fig. 13. Measured total and idle energy per sample as a function of sampling rate. Dashed line shows maximum energy dissipation when C_{STORE} completely discharges.

Fig. 14. Plot showing average ADC output code and nonlinearity versus input pressure.

not optimize the external transceiver for this demonstration—we relied on a commercial single-element transducer, which was designed for 1-MHz operation. In the future, we plan to utilize a phased-array source, designed at 790 kHz, for enhanced beamforming to further decrease the source power consumption. Recently, several papers have been published toward designing phased-arrays for implantable applications [27], [48]–[50].

B. Pressure Sensing Performance

In order to characterize the analog-to-digital signal path, we varied pressure using the syringe pump and compared the wirelessly measured implant samples with the wired reference sensor. We collected 100 samples at each pressure value in order to evaluate the implantable sensor's linearity, FS, LSB, and input-referred noise. Fig. 14 shows a plot of the implantable sensor average output code versus the applied pressure, for 27 different pressure points, over a range of 620 to 1070 mmHg. We measured the LSB to be 0.78 mmHg with an absolute pressure sensing range from 400 to 1200 mmHg ($P_{FS} \cong 800$ mmHg).
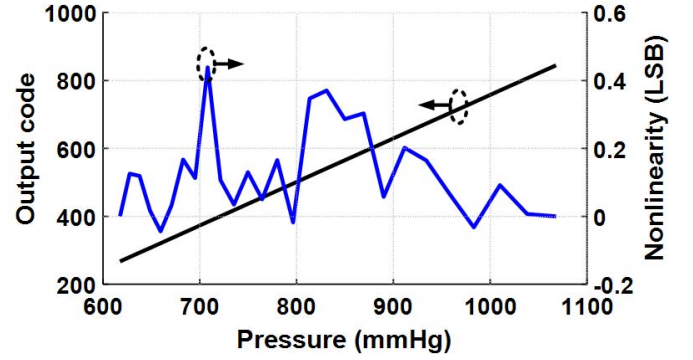
The total sensor nonlinearity, including the PT, AFE, and SAR ADC, was computed using the endpoint method and is also shown in Fig. 14. The implantable sensor shows excellent linearity with worst case nonlinearity of less than 0.44 LSB. The input-referred noise of the front end was measured by computing the standard deviation of the output code using the histogram technique described in [51]. The standard deviation of the output code was measured to be 0.51 LSB, corresponding to an input-referred pressure and voltage noise of 0.4 mmHg and ∼20 µV, respectively. Therefore, an effective number of bits of 9 bits was achieved, giving an effective pressure resolution of ±0.78 mmHg. In order to demonstrate the dynamic functionality of the implant, we also performed time-varying pressure ramps using the pressure setup. Fig. 15 shows a pressure ramp from 780 to 870 mmHg, and back to 780 mmHg with 5-s ramps. The implant measured at 1 ksps and shows excellent agreement with the precise reference sensor.

VIII. FULLY PACKAGED IMPLANT MEASUREMENT

After detailed characterization of the implantable sensor using the setup shown in Fig. 11, we integrated all of the
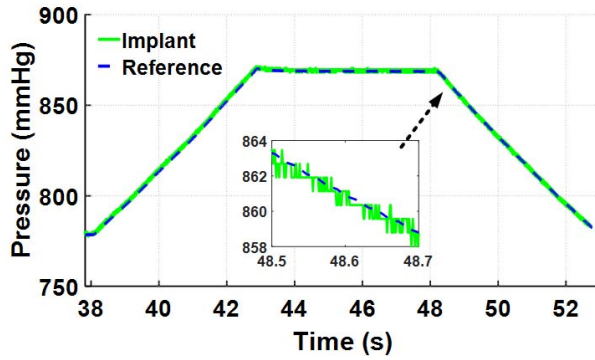
Fig. 15. Measurement comparing implantable sensor versus reference sensor during dynamic pressure ramp.

TABLE I
COMPARISON WITH STATE-OF-THE-ART IMPLANTABLE PRESSURE SENSORS

		This work	[16]-[18]	[19]	[20]
Technology		0.18 μm HV	0.5 μm	1.5 μm	0.18 μm
Modality	power	US	Inductive	Inductive	Inductive
	data	US	RF	RF	Inductive
Size	volume [mm³]	30	417	108 (c)	-
	ratio	x1	x14	x3.6	-
Implant	depth [cm]	12	12	2	2
	medium	Castor oil	unknown (a)	Rat + Air	Air
Depth / volume FoM	[mm⁻²]	4	0.3	0.2	-
Implant energy / sample	[μJ/spl.]	0.28 (< 1 sps) 0.10 (1 ksps)	17.68 (1.5 sps) 2.47 (100 sps)	0.30	21.60
Sample rate	[sps]	0-1000	1.5-100	1000	1
Pressure resolution [mmHg]		0.78	0.6 (>2mHz)(b) 6.3 (0-2mHz)	0.125	0.176
Pressure range [mmHg]		800	1600	~250 (d)	-

(a) Authors performed animal tests at 8-13 cm in [18], but information on link measurements is not available. (b) Does not include noise. (c) Estimated dimensions from figure. (d) Estimated range from figure.

implant components into a single package to verify complete system functionality. All components were assembled onto a flexible polyimide PCB and encapsulated in Polydimethyl-siloxane for biocompatibility. Fig. 16(a) shows a picture of the fully packaged implant, measuring just $1.7 \times 2.3 \times 7.8$ mm³ with the major components annotated. The fully packaged implant was placed into a castor oil tank, and we performed fully wireless testing through 12 cm of castor oil with access to only the external transmitter and receiver. Alignment of the external transmitter and receiver were performed by max-imizing the amplitude of the US backscatter signal. The output power of the transmitter was then increased until we received output codes via the uplink. An example measurement of the transmitted US power burst ($V_{POWER,TX}$) and the corresponding received $V_{DATA,RX}$ are shown in Fig. 16(b). The $V_{DATA,RX}$ waveform clearly shows the US backscatter, which is reflected from the implant during US power-up, the combined echo wait, setup, and sensing time, and lastly the US
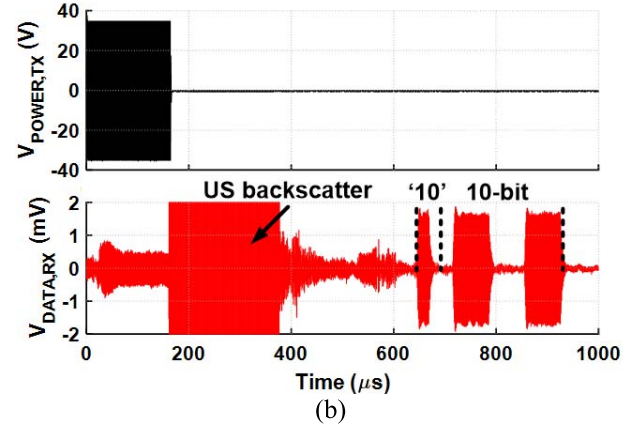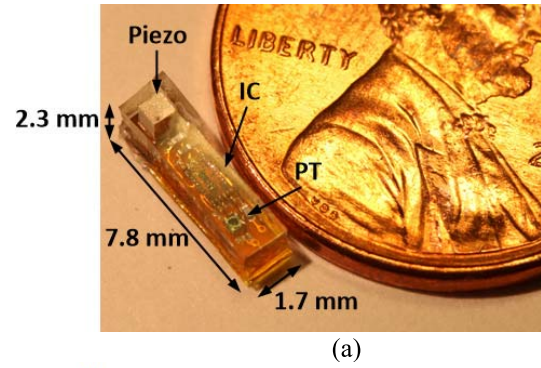

Fig. 16. (a) Picture of fully packaged implant $1.7 \times 2.3 \times 7.8$ mm³. (b) Example measurement of US transmitted power and US uplink waveform from fully packaged measurement—the code is 455.

data uplink. This measurement is in agreement with the mod-ular measurement shown in Fig. 12, confirming operation of the fully packaged implant. We further tested the TM scheme's effectiveness in mitigating US echo coupling to the PT during sampling by varying the US burst power and T_{CHARGE}. In all cases, we found no influence of these parameters on the output word average value or standard deviation, confirming that US coupling is averted during sampling.

Table I compares the performance metrics of this paper with state of the art fully wireless implantable pressure sensors. The advantages of fully ultrasonic links allows for $> 13\times$ improvement in the depth/volume FoM while still achieving a high 30-dB SNR in data uplink. In addition, our implantable sensor is capable of a wide range of tunable sampling rate. Due to our fully external control of f_s, minimizing implant energy dissipation in the idle state, we show a $> 60\times$ decrease in the implant energy per sample for low sampling rates (~ 1 sps).

IX. CONCLUSION

A high-precision implantable pressure sensor with ultrasonic power-up and data uplink was demonstrated. Circuit and system design techniques were presented to enable for both power recovery and data uplink using a single piezoelectric transducer. An energy harvesting analysis of the transient charging of the storage capacitor was presented in order to derive piezo impedance and charging parameters for high-power recovery efficiency. The measured pressure range and resolution exceed specifications required

for most major pressure sensing applications. In addition, the pressure sampling rate is controlled externally, up to 1 ksps, negating the need for continuously running timing and control circuitry on the implant, allowing for lower implant energy consumption and adaptable tuning. The fully packaged implant measures just $1.7 \times 2.3 \times 7.8 \text{ mm}^3$ and was demonstrated at 12 cm in a tissue phantom, while achieving a high SNR data uplink. This paper achieves a $> 13\times$ improvement over state of the art in the depth/volume FoM for implantable pressure sensors.

Acknowledgment

References

[1] L. Minor. (2016). *We Don't Just Need Precision Medicine, We Need Precision Health*. Accessed: Aug. 7, 2017. [Online]. Available: https://www.forbes.com/sites/valleyvoices/2016/01/06/we-dont-just-need-precision-medicine-we-need-precision-health/#6be73476a92f

[2] J. Dusheck. (2016). *A Health-Care Revolution in the Making*. Accessed: Aug. 7, 2017. [Online]. Available: https://stanmed.stanford.edu/2016fall/the-future-of-health-care-diagnostics.html

[3] L. Yu, B. J. Kim, and E. Meng, "Chronically implanted pressure sensors: Challenges and state of the field," *Sensors*, vol. 14, no. 11, pp. 20620–20644, 2014.

[4] I. Clausen and T. Glott, "Development of clinically relevant implantable pressure sensors: Perspectives and challenges," *Sensors*, vol. 14, no. 9, pp. 17686–17702, 2014.

[5] G. Jiang, "Design challenges of implantable pressure monitoring system," *Frontiers Neurosci.*, vol. 4, no. 29, pp. 2–5, 2010.

[6] E. Y. Chow, A. L. Chlebowski, S. Chakraborty, W. J. Chappell, and P. P. Irazoqui, "Fully wireless implantable cardiovascular pressure monitor integrated with a medical stent," *IEEE Trans. Biomed. Eng.*, vol. 57, no. 6, pp. 1487–1496, Jun. 2010.

[7] M. N. Dakurah, C. Koo, W. Choi, and Y.-H. Joung, "Implantable bladder sensors: A methodological review," *Int. Neurourol. J.*, vol. 19, no. 3, pp. 133–141, 2015.

[8] M. H. Ghaed *et al.*, "Circuits for a cubic-millimeter energy-autonomous wireless intraocular pressure monitor," *IEEE Trans. Circuits Syst. I Reg. Papers*, vol. 60, no. 12, pp. 3152–3162, Dec. 2013.

[9] D. Han, Y. Zheng, R. Rajkumar, G. S. Dawe, and M. Je, "A 0.45 V 100-channel neural-recording IC with Sub-μW/channel consumption in 0.18 μm CMOS," *IEEE Trans. Biomed. Circuits Syst.*, vol. 7, no. 6, pp. 735–746, Dec. 2013.

[10] V. Karkare, S. Gibson, and D. Marković, "A 75-μW, 16-channel neural spike-sorting processor with unsupervised clustering," *IEEE J. Solid-State Circuits*, vol. 48, no. 9, pp. 2230–2238, Sep. 2013.

[11] S. B. Lee, B. Lee, M. Kiani, B. Mahmoudi, R. Gross, and M. Ghovanloo, "An inductively-powered wireless neural recording system with a charge sampling analog front-end," *IEEE Sensors J.*, vol. 16, no. 2, pp. 475–484, Jan. 2016.

[12] R. Müller *et al.*, "A minimally invasive 64-channel wireless μECoG implant," *IEEE J. Solid-State Circuits*, vol. 50, no. 1, pp. 344–359, Jan. 2015.

[13] A. DeHennis, S. Getzlaff, D. Grice, and M. Mailand, "An NFC-enabled CMOS IC for a wireless fully implantable glucose sensor," *IEEE J. Biomed. Health Inform.*, vol. 20, no. 1, pp. 18–28, Jan. 2016.

[14] F. Xu, G. Yan, K. Zhao, L. Lu, J. Gao, and G. Liu, "A wireless capsule system with ASIC for monitoring the physiological signals of the human gastrointestinal tract," *IEEE Trans. Biomed. Circuits Syst.*, vol. 8, no. 6, pp. 871–880, Dec. 2014.

[15] H. Cao *et al.*, "An implantable, batteryless, and wireless capsule with integrated impedance and pH sensors for gastroesophageal reflux monitoring," *IEEE Trans. Biomed. Eng.*, vol. 59, no. 11, pp. 3131–3139, Nov. 2012.

[16] S. J. A. Majerus, S. L. Garverick, M. A. Suster, P. C. Fletter, and M. S. Damaser, "Wireless, ultra-low-power implantable sensor for chronic bladder pressure monitoring," *ACM J. Emerg. Technol. Comput. Syst.*, vol. 8, no. 2, 2012, Art. no. 11.

[17] S. Majerus, S. L. Garverick, and M. S. Damaser, "Wireless battery charge management for implantable pressure sensor," in *Proc. IEEE Dallas Circuits Syst. Conf. (DCAS)*, Oct. 2014, pp. 1–5.

[18] S. Majerus, I. Makovey, H. Zhui, W. Ko, and M. S. Damaser, "Wireless implantable pressure monitor for conditional bladder neuromodulation," in *Proc. IEEE Biomed. Circuits Syst. Conf. (BioCAS)*, Oct. 2015, pp. 1–4.

[19] P. Cong, N. Chaimanonart, W. H. Ko, and D. J. Young, "A wireless and batteryless 10-bit implantable blood pressure sensing microsystem with adaptive RF powering for real-time laboratory mice monitoring," *IEEE J. Solid-State Circuits*, vol. 44, no. 12, pp. 3631–3644, Dec. 2009.

[20] J. H. Cheong *et al.*, "An inductively powered implantable blood flow sensor microsystem for vascular grafts," *IEEE Trans. Biomed. Eng.*, vol. 59, no. 9, pp. 2466–2475, Sep. 2012.

[21] P. Cong, W. H. Ko, and D. J. Young, "Wireless batteryless implantable blood pressure monitoring microsystem for small laboratory animals," *IEEE Sensors J.*, vol. 10, no. 2, pp. 243–254, Feb. 2010.

[22] H. Bhamra, J.-W. Tsai, Y.-W. Huang, Q. Yuan, and P. Irazoqui, "A sub-mm^3 wireless implantable intraocular pressure monitor microsystem," in *Proc. IEEE Int. Solid-State Circuits Conf.*, Feb. 2017, pp. 356–357.

[23] A. Donida *et al.*, "A circadian and cardiac intraocular pressure sensor for smart implantable lens," *IEEE Trans. Biomed. Circuits Syst.*, vol. 9, no. 6, pp. 777–789, Dec. 2015.

[24] S. Oh *et al.*, "A dual-slope capacitance-to-digital converter integrated in an implantable pressure-sensing system," *IEEE J. Solid-State Circuits*, vol. 50, no. 7, pp. 1581–1591, Jul. 2015.

[25] M. W. A. Khan, L. Sydänheimo, L. Ukkonen, and T. Björninen, "Inductively powered pressure sensing system integrating a far-field data transmitter for monitoring of intracranial pressure," *IEEE Sensors J.*, vol. 17, no. 7, pp. 2191–2197, Apr. 2017.

[26] M. M. Ghanbari, J. M. Tsai, A. Nirmalathas, R. Müller, and S. Gambini, "An energy-efficient miniaturized intracranial pressure monitoring system," *IEEE J. Solid-State Circuits*, vol. 52, no. 3, pp. 720–734, Mar. 2017.

[27] F. Mazzilli, C. Lafon, and C. Dehollain, "A 10.5 cm ultrasound link for deep implanted medical devices," *IEEE Trans. Biomed. Circuits Syst.*, vol. 8, no. 5, pp. 738–750, Oct. 2014.

[28] P. Gélat, G. ter Haar, and N. Saffari, "The optimization of acoustic fields for ablative therapies of tumours in the upper abdomen," *Phys. Med. Biol.*, vol. 57, no. 24, pp. 8471–8497, 2012.

[29] J. W. Hand, A. Shaw, N. Sadhoo, S. Rajagopal, R. J. Dickinson, and L. R. Gavrilov, "A random phased array device for delivery of high intensity focused ultrasound," *Phys. Med. Biol.*, vol. 54, no. 19, pp. 5675–5693, 2009.

[30] T. C. Chang, M. J. Weber, M. L. Wang, J. Charthad, B. Pierre T. Khuri-Yakub, and A. Arbabian, "Design of tunable ultrasonic receivers for efficient powering of implantable medical devices with reconfigurable power loads," *IEEE Trans. Ultrason. Ferroelect. Freq. Control*, vol. 63, no. 10, pp. 1554–1562, Oct. 2016.

[31] J. Charthad, M. J. Weber, T. C. Chang, and A. Arbabian, "A mm-sized implantable medical device (IMD) with ultrasonic power transfer and a hybrid bi-directional data link," *IEEE J. Solid-State Circuits*, vol. 50, no. 8, pp. 1741–1753, Aug. 2015.

[32] M. J. Weber, A. Bhat, T. C. Chang, J. Charthad, and A. Arbabian, "A miniaturized ultrasonically powered programmable optogenetic implant stimulator system," in *Proc. IEEE Topical Conf. Biomed. Wireless Technol., Netw., Sens. Syst. (BioWireleSS)*, Jan. 2016, pp. 12–14.

[33] M. O. Culjat, D. Goldenberg, P. Tewari, and R. S. Singh, "A review of tissue substitutes for ultrasound imaging," *Ultrasound Med. Biol.*, vol. 36, no. 6, pp. 861–873, Jun. 2010.

[34] P. J. Larson and B. C. Towe, "Miniature ultrasonically powered wireless nerve cuff stimulator," in *Proc. 5th Int. IEEE/EMBS Conf. Neural Eng.*, Apr./May 2011, pp. 265–268.

[35] Y.-S. Luo *et al.*, "Ultrasonic power/data telemetry and neural stimulator with OOK-PM signaling," *IEEE Trans. Circuits Syst. II, Exp. Briefs*, vol. 60, no. 12, pp. 827–831, Dec. 2013.

[36] D. Seo *et al.*, "Wireless recording in the peripheral nervous system with ultrasonic neural dust," *Neuron*, vol. 91, no. 3, pp. 529–539, 2016.

[37] T. Maleki, N. Cao, S. H. Song, C. Kao, S.-C. Ko, and B. Ziaie, "An ultrasonically powered implantable micro-oxygen generator (IMOG)," *IEEE Trans. Biomed. Eng.*, vol. 58, no. 11, pp. 3104–3111, Nov. 2011.

[38] T. C. Chang, M. L. Wang, J. Charthad, M. J. Weber, and A. Arbabian, "A 30.5 mm³ fully packaged implantable device with duplex ultrasonic data and power links achieving 95 kb/s with <10-4 BER at 8.5 cm depth," in *Proc. IEEE Int. Solid-State Circuits Conf.*, Feb. 2017, pp. 460–461.

[39] M. J. Weber *et al.*, "A high-precision 36 mm³ programmable implantable pressure sensor with fully ultrasonic power-up and data link," in *Proc. Symp. VLSI Circuits*, Jun. 2017, pp. 104–105.

[40] J. Charthad, N. Dolatsha, A. Rekhi, and A. Arbabian, "System-level analysis of far-field radio frequency power delivery for mm-sized sensor nodes," *IEEE Trans. Circuits Syst. I, Reg. Papers*, vol. 63, no. 2, pp. 300–311, Feb. 2016.

[41] R. E. Barnett, J. Liu, and S. Lazar, "A RF to DC voltage conversion model for multi-stage rectifiers in UHF RFID transponders," *IEEE J. Solid-State Circuits*, vol. 44, no. 2, pp. 354–370, Feb. 2009.

[42] A. Arbabian *et al.*, "Sound technologies, sound bodies: Medical implants with ultrasonic links," *IEEE Microw. Mag.*, vol. 17, no. 12, pp. 39–54, Dec. 2016.

[43] G. S. Kino, *Acoustic Waves: Devices, Imaging, and Analog Signal Processing*. Englewood Cliffs, NJ, USA: Prentice-Hall, 1987.

[44] H. Tian and A. El Gamal, "Analysis of 1/f noise in switched MOSFET circuits," *IEEE Trans. Circuits Syst. II, Analog Digit. Signal Process.*, vol. 48, no. 2, pp. 151–157, Feb. 2001.

[45] V. Tripathi and B. Murmann, "An 8-bit 450-MS/s single-bit/cycle SAR ADC in 65-nm CMOS," in *Proc. Eur. Solid-State Circuits Conf.*, Sep. 2013, pp. 117–120.

[46] V. Tripathi and B. Murmann, "Mismatch characterization of small metal fringe capacitors," *IEEE Trans. Circuits Syst. I, Reg. Papers*, vol. 61, no. 8, pp. 2236–2242, Aug. 2014.

[47] D. L. Miller, "Safety assurance in obstetrical ultrasound," *Semin. Ultrasound, CT MRI*, vol. 29, no. 2, pp. 156–164, 2008.

[48] M. L. Wang, T. C. Chang, T. Teisberg, M. J. Weber, J. Charthad, and A. Arbabian, "Closed-loop ultrasonic power and communication with multiple miniaturized active implantable medical devices," in *Proc. IEEE Int. Ultrason. Symp.*, Sep. 2017, pp. 1–4.

[49] B. Cotte, C. Lafon, C. Dehollain, and J.-Y. Chapelon, "Theoretical study for safe and efficient energy transfer to deeply implanted devices using ultrasound," *IEEE Trans. Ultrason. Ferroelect. Freq. Control*, vol. 59, no. 8, pp. 1674–1685, Aug. 2012.

[50] D. Seo *et al.*, "Ultrasonic beamforming system for interrogating multiple implantable sensors," in *Proc. IEEE Int. Conf. Eng. Med. Biol. Soc.*, Aug. 2015, pp. 2673–2676.

[51] S. Ruscak and L. Singer, "Using histogram techniques to measure A/D converter noise," *Analog Dialogue*, vol. 29, no. 2, pp. 7–8, 1995.

Yoshiaki Yoshihara (M'09) received the B.E. degree in electronical and electronics engineering and the M.E. degree in advanced applied electronics from the Tokyo Institute of Technology, Tokyo, Japan, in 2003 and 2005, respectively.

In 2005, he joined Toshiba Corporation, Kawasaki, Japan, where he was involved in the research and development of wireless communication circuits. From 2016 to 2017, he was a Visiting Scholar at Stanford University, Stanford, CA, USA, where he was involved in research of implantable medical devices. In 2017, he joined Toshiba Memory Corporation, Kawasaki. His current research interests include wireline communication and chip-package-system co-design for memory systems.

Ahmed Sawaby (S'17) received the B.S. and M.S. degrees in electrical engineering from Cairo University, Giza, Egypt, in 2014 and 2017, respectively. He is currently pursuing the Ph.D. degree with Stanford University, Stanford, CA, USA.

From 2014 to 2015, he was with Cairo Circuits and Systems Lab, Cairo, Egypt, where he designed high-speed DACs for a frequency hopping transmitter front end. From 2015 to 2016, he was with Silicon Vision, Cairo, as an RF Design Engineer, where he was involved in designing the PMU of Synopsys's state-of-the-art 55-nm Bluetooth Low Energy IP. In 2016–2017, he was with the Arbabian Lab, Stanford University, as a Visiting Student, where he focused on implantable medical chips.

Mr. Sawaby was a recipient of the Stanford Graduate Fellowship.

Jayant Charthad (S'13) received the B.Tech. degree in electrical engineering from IIT Bombay, Mumbai, India, in 2009, and the M.S. degree in electrical engineering from Stanford University, Stanford, CA, USA, in 2013, where he is currently pursuing the Ph.D. degree in electrical engineering.

From 2009 to 2011, he was with Texas Instruments, Bangalore, India, where he designed low-dropout regulator ICs. In 2012, he was with the SAR ADC team at Linear Technology, Milpitas, CA, USA. His current research interests include wireless power transfer, implantable medical devices, bio-sensing, and integrated circuit and system design.

Mr. Charthad was a recipient of the Analog Devices Outstanding Student Designer Award in 2014, the Centennial Teaching Assistant Award in 2015, and the 2015 James F. Gibbons Outstanding Student Teaching Award in Electrical Engineering at Stanford University.

Marcus J. Weber (S'10) received the B.S. degree in electrical engineering from the University of Wisconsin–Madison, Madison, WI, USA, in 2012, and the M.S. degree in electrical engineering from Stanford University, Stanford, CA, USA, in 2014, where he is currently pursuing the Ph.D. degree in electrical engineering.

In 2008, he was a Software Engineering Intern with GE Healthcare, Milwaukee, WI, USA. He was an Electrical Engineer in three cooperative education semesters at NASA Johnson Space Center, Houston, TX, USA, from 2009 to 2011. From 2010 to 2012, he was with the University of Wisconsin–Madison, where he researched the atmospheric effects on terahertz wave propagation. His current research interests include implantable devices, bio-sensing, wireless power and communication, energy harvesting, low-power electronics, and analog and RF circuit design.

Mr. Weber was a recipient of the Stanford Graduate Fellowship, the National Science Foundation Graduate Research Fellowship, the Best Paper Award at the 2016 IEEE Conference on Biomedical Wireless Technologies, Networks, and Sensing Systems, and the Fairchild Semiconductor Student Designer Award.

Ting Chia Chang (S'11) received the B.S. degree in electrical engineering and computer sciences from the University of California at Berkeley, Berkeley, CA, USA, in 2012, and the M.S. degree in electrical engineering from Stanford University, Stanford, CA, USA, in 2015, where he is currently pursuing the Ph.D. degree in electrical engineering.

In 2011, he was an Intern at the Microelectronic Research Center, University of Texas at Austin, Austin, TX, USA. His current research interests include wireless power delivery, wireless communication, acoustics applications, implantable medical devices, and digital and analog low-power integrated circuit design.

Mr. Chang was a recipient of Honorable Mentions from National Science Foundation Graduate Research Fellowship in 2014, the Analog Device Outstanding Student Design Award in 2017, and the Best Paper Award in IEEE BIOCAS Conference in 2017.

Amin Arbabian (S'06–M'12–SM'17) received the Ph.D. degree in electrical engineering and computer science from the University of California at Berkeley, Berkeley, CA, USA, in 2011.

From 2007 to 2008, he was with the Initial Engineering Team, Tagarray, Inc., Palo Alto, CA, USA. He was with Qualcomm's Corporate Research and Development Division, San Diego, CA, USA, in 2010, where he designed circuits for next-generation ultralow-power wireless transceivers. In 2012, he joined Stanford University, Stanford, CA, USA, as an Assistant Professor of electrical engineering. He is currently a Frederick E. Terman Fellow with the School of Engineering. His current research interests include high-frequency systems, medical imaging, Internet-of-Everything devices including wireless power delivery techniques, and medical implants.

Dr. Arbabian was a recipient or co-recipient of the 2016 Stanford University Tau Beta Pi Award for Excellence in Undergraduate Teaching, the 2015 NSF CAREER Award, the 2014 DARPA Young Faculty Award including the Director's Fellowship in 2016, the 2013 Hellman Faculty Scholarship, the 2010–2011, 2014–2015, and 2016–2017 Qualcomm Innovation Fellowships, the 2010 IEEE Jack Kilby Award for Outstanding Student Paper at the IEEE International Solid-State Circuits Conference, and two time second place best student paper awards at 2008 and 2011 RFIC symposiums, and best paper awards at the 2017 IEEE Biomedical Circuits and Systems Conference, the 2016 IEEE Conference on Biomedical Wireless Technologies, Networks, and Sensing Systems, the 2014 IEEE VLSI Circuits symposium, and the 2013 IEEE International Conference on Ultra-Wideband. He currently serves on the steering committee of RFIC Symposium, the technical program committees of RFIC symposium, ESSCIRC, and VLSI Circuits Symposium, and as an Associate Editor of the IEEE SOLID-STATE CIRCUITS LETTERS and the IEEE JOURNAL OF ELECTROMAGNETICS, RF AND MICROWAVES IN MEDICINE AND BIOLOGY.